Computers and Geotechnics 116 (2019) 103188

Contents lists available at ScienceDirect

Computers and Geotechnics

journal homepage: www.elsevier.com/locate/compgeo

Research Paper

Can we estimate far-field stress using the mean of local stresses? An examination based on numerical simulations

Ke Gao[a], Qinghua Lei[b,*], Nezam Bozorgzadeh[c], Viet Chau[a]

[a] Geophysics, Los Alamos National Laboratory, Los Alamos, USA
[b] Department of Earth Sciences, ETH Zürich, Zürich, Switzerland
[c] GeoEngineering Centre, Department of Civil Engineering, Royal Military College of Canada, Kingston, Canada

ARTICLE INFO

Keywords:
Stress tensor
Far-field stress
Euclidean mean
Stress variability

ABSTRACT

In situ stress is an important parameter in rock mechanics, and reliable estimates of far-field stresses are indispensable for robust rock engineering analysis. Here, by using the combined finite-discrete element method, we simulate a series of stress fields of both synthetic and natural fracture networks to examine whether the Euclidean mean of local stresses can be used to estimate the far-field stress. The calculations show that given a large number of local stress measurements, their Euclidean mean gives a close approximation of the far-field stress state. Whereas when only a limited number of local stresses are available, the probability of obtaining a practically acceptable estimate of far-field stress increases when more stress measurements are involved. The required number of stress measurements for deriving an acceptable estimate varies with the geomechanical condition; in general, the larger the overall stress variability is, the more local stress measurements are needed. Our research findings suggest that given a limited number of stress measurements, which is often encountered in rock engineering projects, attention is needed when deriving the far-field stress state based on them, and simply using their mean as far-field stress for further rock structure design and numerical analysis may yield erroneous results.

1. Introduction

Rock masses are stressed in their natural state, mainly due to the overburden and tectonic effects [1]. The understanding of the *in situ* stress state is thus important for many rock mechanics problems, including geotechnical engineering design, hydraulic fracturing analysis, rock mass permeability, and earthquake potential evaluation [1–4]. Given the fact that the far-field stresses related to plate-driving forces are typically uniform over the lithospheric scale [5], in such stress-related applications, it is common to assume in many analytical methods and numerical simulations that the problem domain of interest is subjected to far-field stress loadings such that the response of rock masses associated with geological features (e.g. folds, faults, intrusions) or artificial structures (e.g. tunnels, caverns, mines, surface excavations) is further analyzed [6–12]. One succinct example is the use of Kirsch solution to calculate the stress distribution around a circular opening inside a rock medium sustaining far-field stresses [13]. Thus, the far-field stress state is an important input parameter for many rock mechanics analyses [3,7,8,14–17], and reliable estimate of it is indispensable for robust evaluation of rock mass behavior.

The far-field stress state of a geological investigation region is often interpreted by referring to the local stress measurements. However, due to the inherent heterogeneity and anisotropy of fractured rock masses, the *in situ* stress field often displays significant variability [18–24], and so the relationship between far-field stress and local stresses is obscured. Particularly, it is not clear if a reliable estimate of far-field stress can be attained when facing the common rock engineering situation where only a limited number of local *in situ* stress measurements are available. Therefore, it is essential that a systematic study of this problem can be conducted.

Here, using the tensor-based mean stress calculation approach – Euclidean mean – developed earlier [25–27] and the hybrid finite-discrete element method (FDEM) [28], we simulate and analyze the stress fields of different fractured rock mass systems based on synthetic and natural fracture networks. We examine whether the Euclidean mean of local stresses in a rock mass can be used as an acceptable estimate of the far-field stress. A major benefit of this approach is that we can fully resolve the local stress field with respect to various prescribed far-field stress conditions, which allows us to elucidate their interrelationship quantitatively and systematically. In this study, we focus on the two-

* Corresponding author.
E-mail address: qinghua.lei@erdw.ethz.ch (Q. Lei).

https://doi.org/10.1016/j.compgeo.2019.103188
Received 16 February 2019; Received in revised form 21 June 2019; Accepted 29 July 2019
0266-352X/ © 2019 Elsevier Ltd. All rights reserved.

dimensional (2D) analysis, which is applicable for cases such as sedimentary formations whose longitudinal characteristic scale is much larger than their transversal one. We assume that the *in situ* stress field in the fractured rock develops entirely based on the imposed contemporary tectonic stresses, whereas the possible residual stress effect is omitted.

In the following sections, we first give a brief description of the FDEM method, the generation of synthetic and natural fracture networks, and the Euclidean mean stress calculation approach. Then, we calculate the Euclidean mean of all the simulated local stress tensors in each simulation, and compare it with the prescribed far-field stress to examine their equality. Further, we randomly sample a certain number of local stresses and compare their mean with the far-field stresses to investigate how reliable the Euclidean mean of local stresses is for far-field stress estimation and how it depends on the sampling size. Finally, we aim to provide suggestions for estimating appropriate far-field stress in practical rock engineering applications.

2. Stress computation and analysis approaches

2.1. Numerical method for stress computation

The local stress data for mean stress calculation and comparison with far-field stress in the present study are obtained from a series of numerical simulations, which use a 2D FDEM model to determine how stresses are distributed in fractured rock masses when subjected to different far-field stresses. The FDEM method was originally developed by Munjiza and his colleagues, which combines the advantages of both the finite element method (FEM) and discrete element method (DEM) [28–33]. In FDEM, the FEM module simulates continuum problems (e.g. stress and strain) and the DEM module handles discontinuum processes (e.g. contact and interaction) (Fig. 1) [28]. In the FDEM framework, a 2D fractured rock mass is represented using a fully discontinuous mesh of three-node triangular finite elements, which are linked by four-node crack elements (Fig. 1).

The motions of finite elements are governed by the forces acting on elemental nodes. The governing equation is given by [28]:

$$\mathbf{M}\ddot{\mathbf{x}} + \mathbf{f}_{\text{int}} = \mathbf{f}_{\text{ext}}, \tag{1}$$

where $\mathbf{M}$ is the lumped nodal mass matrix, $\mathbf{x}$ is the vector of nodal displacements, $\mathbf{f}_{\text{int}}$ are the internal nodal forces induced by the deformation of triangular elements, $\mathbf{f}_{\text{ext}}$ are the external nodal forces including external loads $\mathbf{f}_{\text{a}}$ contributed by boundary conditions and body forces, cohesive bonding forces $\mathbf{f}_{\text{b}}$ caused by the deformation of crack elements, and contact forces $\mathbf{f}_{\text{c}}$ generated by the contact interaction between adjacent elements located along two sides of fractures. The equations of motion of the FDEM system are solved by an explicit time integration scheme based on the forward Euler method.

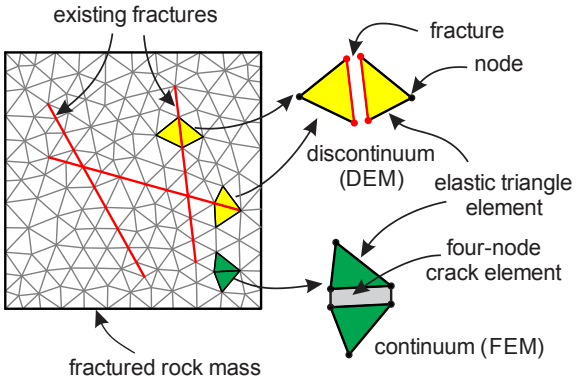

Fig. 1. Schematic illustration of FEM and DEM modules in FDEM. The triangular elements along two sides of the fracture are treated as discrete elements, while other places are handled in a finite element manner with a four-node crack element inserted between adjacent triangular elements [23].

The intact rock is assumed to be isotropic and homogeneous, and a Mohr-Coulomb model with tension cut-off is employed to define its shear and tensile strength [34]. The deformation of the bulk material is captured by the linear-elastic constant-strain triangular finite elements with the impenetrability enforced by a penalty function and the continuity constrained by bonding forces of crack elements [35]. FDEM allows explicit geometric realization of fracture patterns. Particularly, the embedded combined single and smeared crack model permits the simulator to capture the emergence of new fractures driven by stress concentrations [35], which eliminates unrealistic stress singularities at fracture tips and thus makes it an ideal tool for stress computation [23]. Some limitations may be present in FDEM simulation. For example, the results of fracture initiation and propagation are constrained by elemental edges and may thus be affected by mesh discretization. To minimize such an effect, we choose an element size that is small enough to suppress the potential mesh-dependency via mesh sensitivity analysis. The accuracy of FDEM for stress simulation has been validated in our previous work [24], which shows great agreements with analytical solutions for stress distribution around single fracture under various far-field loadings.

2.2. Numerical model setup

2.2.1. The synthetic fracture networks

We simulate the geometry of fracture networks in granitic rocks using the synthetic fracture network model following a power-law length scaling given by [36]:

$$n(l, L) = \alpha L^{D} l^{-a}, \text{ for } l \in [l_{\min}, l_{\max}], \tag{2}$$

where $n(l, L)dl$ is the number of fractures with sizes l belonging to the interval $[l, l + dl](dl \ll l)$ in an elementary volume of characteristic size L, D is the fractal dimension, a is the power-law length exponent, and α is the density term. The only intrinsic characteristic length scales in this model are the smallest and largest fracture lengths, i.e. $l_{\min}$ and $l_{\max}$, respectively. In numerical simulations, L is the scale of the modeling domain, which usually meets $l_{\min} \ll L \ll l_{\max}$. The exponents D and a quantify different scaling aspects of fracture networks: the fracture density (related to D) and the length distribution (related to a). Extensive outcrop data suggest that generally D varies between 1.5 and 2.0, and a falls between 1.3 and 3.5 [36]. Fracture intensity is defined as the total length of fractures per unit area. The mean fracture intensity $\bar{\gamma}$ of a fracture network within a square domain of size L is calculated as:

$$\bar{\gamma} = \frac{1}{L^2} \int_{A_L} n(l, L) l' dl \tag{3}$$

where l' denotes the fracture length included in the domain of an area $A_L = L^2$.

The 2D models with synthetic fracture networks are generated in a square domain of size $L = 10$ m (Fig. 2), in which the location and orientation of fractures are assumed to be completely random, i.e. nominally homogeneous (i.e. $D = 2.0$) and isotropic. The bounds of fracture lengths are given by $l_{\min} = L/50 = 0.2$ m and $l_{\max} = 50L = 500$ m. We explore five different length exponent cases, i.e. $a = 1.5$, 2.0 2.5, 3.0 and 3.5, and two different mean fracture intensity scenarios, i.e. $\bar{\gamma} = 2.5$ and $5.0\,\text{m}^{-1}$. The generated fracture networks are presented in Fig. 2. For small a, the rock mass is dominated by long fractures. With the increase of a, more short fractures are introduced. Also, when $\bar{\gamma}$ is increased from 2.5 to $5.0\,\text{m}^{-1}$, more densely distributed fractures can be observed. For each combination of a and $\bar{\gamma}$, we generate ten realizations, and thus a total of 100 synthetic fracture rock mass models are created. It is worth mentioning that, to avoid low quality elements in later mesh generation, a set of automated geometrical modification algorithms as proposed by Mayer et al. [37] have been implemented into the synthetic fracture network generator

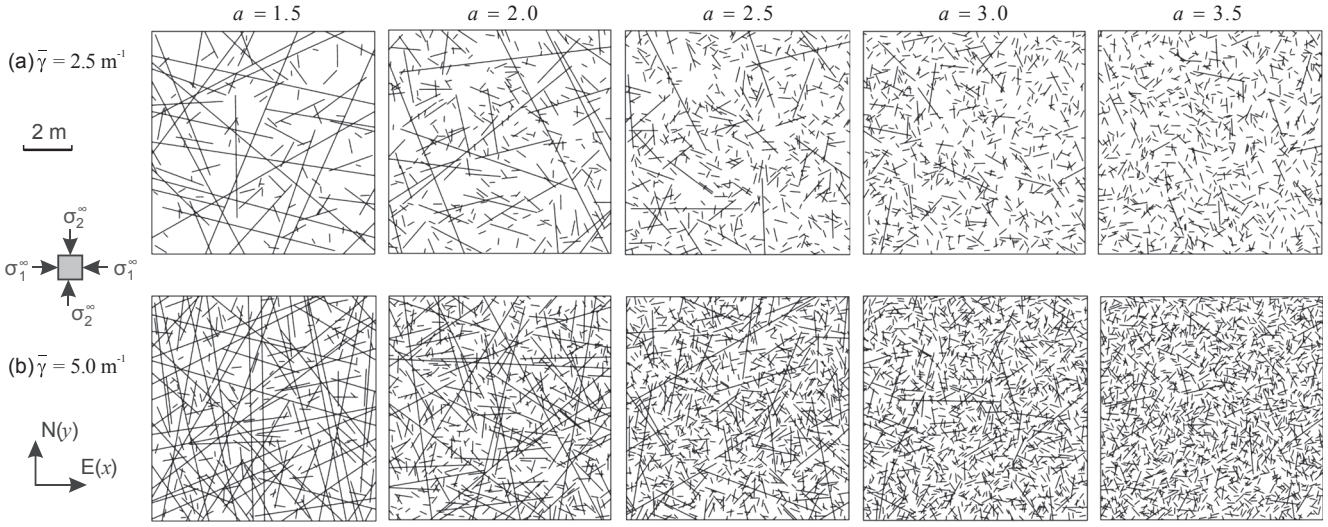

Fig. 2. The geometry of generated synthetic fracture networks in granite (domain size L = 10 m) associated with various power-law length exponent a and mean fracture intensity $\bar{\gamma}$. The small shaded block on the left side indicates the far-field stress imposed on the models.

such that the scenarios of closely spaced fractures and fractures intersecting at tiny angles are eliminated.

The material properties of the granitic rock are assumed as follows [2]: the bulk density is 2,700 kg/m^3, the Young's modulus is 50.0 GPa, the Poisson's ratio is 0.25, the internal friction coefficient is 1.0, the tensile strength is 20.0 MPa, the cohesive strength is 40.0 MPa, and the mode I and II energy release rates are 158.4 and 198.0 J/m^2, respectively. The frictional sliding on fractures obeys the Coulomb criterion with a friction coefficient of $\mu = 0.85$ [38]. A penalty parameter with a value 10 times of the Young's modulus is employed by compromising between achieving the correct elastic response among contacting elements and maximizing the time step size to reduce the overall computational expense. The selected penalty parameter is within the reasonable range according to [28,39]. Each model is discretized using an approximately uniform, unstructured mesh with an average element size of 0.05 m. As a result, a total of more than 70,000 triangular elements have been generated for each model.

Far-field stresses are applied orthogonally to the model boundaries (Fig. 2), and we consider three scenarios: (i) σ_1^∞ = 5.0 MPa, σ_2^∞ = 5.0 MPa, (ii) σ_1^∞ = 10.0 MPa, σ_2^∞ = 5.0 MPa, and (iii) σ_1^∞ = 15.0 MPa, σ_2^∞ = 5.0 MPa, corresponding to stress ratios $\sigma_1^\infty/\sigma_2^\infty$ = 1.0, 2.0, and 3.0, respectively. Here, for simplicity and convenience, we use the orientation of σ_1^∞, denoted by ϕ, to represent the orientation of far-field stress, as the trend of σ_2^∞ can then be acquired accordingly. For the current case in which the σ_1^∞ is acting in the x-direction, when using the geological convention of clockwise positive from North (Fig. 2), the orientation of σ_1^∞ is marked as $\phi = 90^\circ$.

2.2.2. The natural fracture networks

We also construct realistic fracture network models based on a real outcrop of natural fractures, e.g. an 18 m × 18 m outcrop map of a Devonian age sandstone located at the Hornelen Basin, western Norway [40] (Fig. 3a). This fracture pattern consists of more than 2,000 joints which are mostly perpendicular to the bedding and can be grouped into three major sets with their mean set orientations of being 40°, 85° and 150° (clockwise positive from North) (Fig. 3). The formation of this fracture system was interpreted as the result of stress release on uplift and erosion [40].

The material properties of the fractured Hornelen sandstone are assumed as follows [41]: the bulk density is 2,500 kg/m^3, the Young's modulus is 20.0 GPa, the Poisson's ratio is 0.25, the internal friction coefficient is 1.0, the tensile strength is 20.0 MPa, the internal cohesive strength is 40.0 MPa, the joint friction coefficient is 0.85, and the mode I and II energy release rates are 396.1 and 495.1 J/m^2, respectively. The penalty parameter is also chosen to be 10 times of the Young's modulus. The Hornelen model is discretized using an approximately uniform, unstructured triangular meshes with an average element size of 0.075 m (around 108,000 elements in total). The elements size for the Hornelen model is carefully chosen to be small enough to avoid highly skewed triangular elements and also by considering the computation expense and the resolution of the resulting stress data through a series of mesh sensitivity analyses [42].

Same as the synthetic fracture models, three far-field stress scenarios are explored on the Hornelen model: (i) σ_1^∞ = 5.0 MPa, σ_2^∞ = 5.0 MPa, (ii) σ_1^∞ = 10.0 MPa, σ_2^∞ = 5.0 MPa, and (iii) σ_1^∞ = 15.0 MPa, σ_2^∞ = 5.0 MPa. Considering the anisotropy feature of the natural fracture system, we study various far-field stress loading conditions imposed at a range of angles to the domain. First, the σ_1^∞ and σ_2^∞ are acting in the y- and x-direction, respectively, on the model boundaries. Following this, a series of other simulations are conducted by rotating the far-field stresses clockwise for 170° with a step size of 10°, as demonstrated in Fig. 3b. Using the same convention as in the previous section, the orientations of σ_1^∞ for the current simulations are thus ϕ = 0°, 10°, 20°, ...,170°. The far-field stress rotation is implemented by first calculating the stress tensor corresponding to each rotated far-field stress in the x-y coordinate system, then the normal and shear components of the calculated stress tensor are added to the boundaries of the rock mass in the form of normal and shear components, respectively (Fig. 3b). Note that for $\sigma_1^\infty/\sigma_2^\infty$ = 1 (i.e. $\sigma_1^\infty = \sigma_2^\infty$ = 5.0 MPa), no far-field stress rotation is needed. In each simulation, the far-field stresses are imposed uniformly along the boundary of the rock mass via a ramped stage to eliminate dynamic effects. When the model attains equilibrium, stress tensors at each element are extracted for further tensorial analysis.

Additionally, we have conducted simulations on two other natural fracture networks – the Kilve and Bristol models (see Appendix C) – to further examine the conclusions drawn from the Hornelen natural fracture model.

2.3. Euclidean mean stress calculation

In conventional rock stress analysis, stress magnitude and orientation are customarily processed separately [43–47], which essentially decomposes the stress tensor into scalar (principal stress magnitudes) and vector (principal stress orientations) components, and statistically analyses them using classical statistics [48] and directional statistics

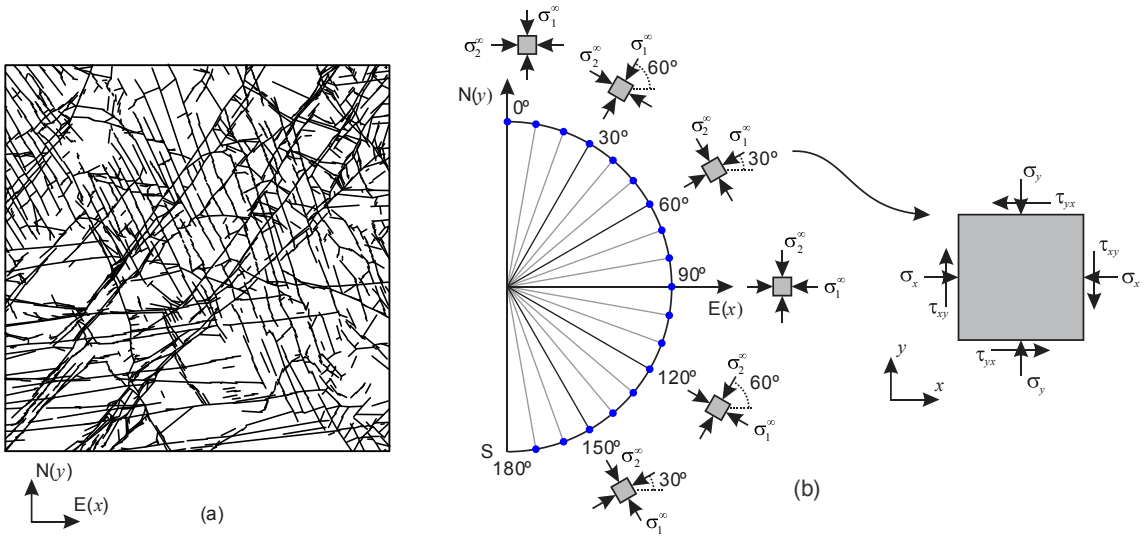

Fig. 3. (a) An 18 m × 18 m outcrop map of the natural fracture system in the Devonian sandstone at Hornelen Basin, western Norway [40]. (b) Schematic description of the far-field stress rotation used in Hornelen model simulations.

[49], respectively. However, it has been demonstrated that this customary scalar/vector approach violates the tensorial nature of stress and may yield erroneous results, especially for the mean stress calculation [27]. One manifest drawback of it is that the orthogonality of calculated mean principal stresses is not guaranteed [27].

Since stress is a second-order tensor, statistical analysis of it should be conducted based on the tensors referred to a common Cartesian coordinate system [50]. By considering the tensorial nature of stress, the mean stress – so-called Euclidean mean – has been derived in a tensorial manner based on the distance measure between stress tensors in Euclidean space [26]. For example, let the *i*th stress tensor $\mathbf{S}_i$ be denoted by

$$\mathbf{S}_i = \begin{bmatrix} \sigma_{x_i} & \tau_{xy_i} \\ sym. & \sigma_{y_i} \end{bmatrix} \tag{4}$$

where σ and τ are the normal and shear components, respectively. Then the Euclidean mean stress can be calculated by averaging each tensor component, i.e.

$$\bar{\mathbf{S}} = \frac{1}{n}\sum_{i=1}^{n}\mathbf{S}_i = \begin{bmatrix} \bar{\sigma}_x & \bar{\tau}_{xy} \\ sym. & \bar{\sigma}_y \end{bmatrix} = \frac{1}{n}\begin{bmatrix} \sum_{i=1}^{n}\sigma_{x_i} & \sum_{i=1}^{n}\tau_{xy_i} \\ sym. & \sum_{i=1}^{n}\sigma_{y_i} \end{bmatrix}, \tag{5}$$

where $\bar{\mathbf{S}}$ denotes the Euclidean mean stress tensor, and $\bar{\sigma}$ and $\bar{\tau}$ are the corresponding mean components.

To facilitate comparison between the calculated Euclidean mean of simulated stress data and the prescribed far-field stress imposed on the rock mass model, the eigenvalues and eigenvectors of the Euclidean mean, which represent the magnitudes and orientations of the principal mean stresses, are calculated. The major and minor principal stress magnitudes of the Euclidean mean are denoted as $\bar{\sigma}_1$ and $\bar{\sigma}_2$, respectively. Also, for convenience, we use the trend of $\bar{\sigma}_1$, denoted by $\bar{\theta}$, to represent the orientation of principal mean stresses. Since $\bar{\theta}$ is bi-directional, to avoid ambiguity, we consider the $\bar{\theta}$ located within the range of $[0,\ \pi]$ (clockwise positive from North).

3. Euclidean mean of all local stresses and its equality with the prescribed far-field stress

3.1. The synthetic fracture models

A total of 300 simulations (100 models × 3 far-field stress scenarios) have been conducted for the synthetic fracture rock mass models. The distributions of local major principal stresses in one of the ten realization sets are shown in Fig. 4. It seems that the distribution of local stresses becomes more heterogeneous with the increase of the far-field stress ratio $\sigma_1^\infty/\sigma_2^\infty$, the decrease of the power-law length exponent *a*, and/or the increase of the mean fracture intensity $\bar{\gamma}$. The Euclidean mean of all stress data in each model is calculated and compared to the prescribed far-field stress. The difference between the Euclidean mean and the far-field stress in terms of major, minor principal stress magnitude and orientation are respectively evaluated by $|\bar{\sigma}_1 - \sigma_1^\infty|/\sigma_1^\infty$, $|\bar{\sigma}_2 - \sigma_2^\infty|/\sigma_2^\infty$ and $|\bar{\theta} - \phi|$, and the magnitude and orientation differences are presented in percentage and degree (°), respectively. The results for the three far-field stress scenarios are given in Fig. 5 with each marker representing the mean of the difference for the ten synthetic fracture realizations corresponding to a specific combination of power-law length exponent *a* and mean fracture intensity $\bar{\gamma}$, and the associated shaded area representing one standard deviation upper and lower with respect to the mean. Note that the orientation difference is not compared for the $\sigma_1^\infty/\sigma_2^\infty = 1$ scenario.

As can be seen from Fig. 5, the magnitude difference between the Euclidean mean of all simulated stresses and the prescribed far-field stress for each synthetic fracture model is less than 5% (most of them are less than 3%) and the orientation difference is less than 0.3°. Larger magnitude and orientation difference generally occurs for the models subjected to higher $\sigma_1^\infty/\sigma_2^\infty$. Slightly larger differences are seen for the models with smaller mean fracture intensity $\bar{\gamma}$ (left panel of Fig. 5). The magnitude difference is not very sensitive with respect to *a* (Fig. 5a–d), while the orientation difference shows a decreasing trend with the increasing *a* (Fig. 5e & f). The difference in terms of minor principal stress magnitude (Fig. 5c & d) is generally larger than that of the major principal stress magnitude (Fig. 5a & b) for $\sigma_1^\infty/\sigma_2^\infty = 2$ and 3. The variation (shown as ± 1 standard deviation, shaded area) of both the magnitude and orientation difference of the ten synthetic fracture realizations for each combination of *a* and $\bar{\gamma}$ mainly decreases with the increasing *a*, and has larger values for larger $\sigma_1^\infty/\sigma_2^\infty$. Nevertheless, the small difference between the Euclidean mean and the prescribed far-field stress for the synthetic fracture models demonstrates that they can be practically deemed as equivalent.

The difference between the Euclidean mean of all simulated stresses and the prescribed far-field stress may be related to the overall stress variability. To examine this postulation, we calculate the effective variance of all the simulated stresses – a scalar-valued measure of overall stress variability [51] – for each model. A detailed description of the effective variance is given in Appendix B. The higher the effective variance is, the more spread out a stress data group is with respect to

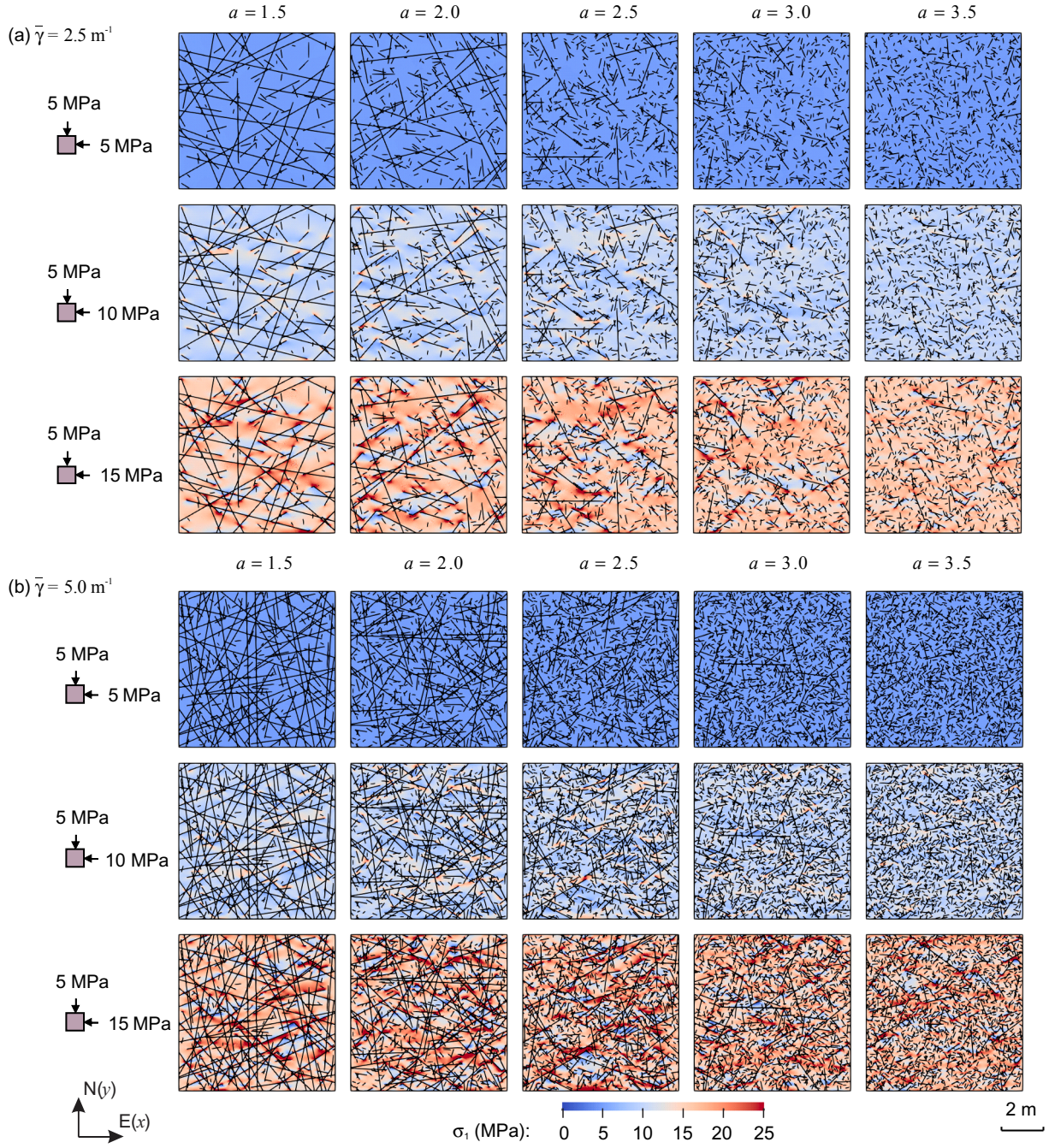

Fig. 4. Distributions of local major principal stresses in one of the ten realization sets of the synthetic fracture rock mass models.

their mean and thus larger overall stress variability. The effective variances of the simulated stresses for each synthetic fracture model are presented in Fig. 6. Similarly, the markers in Fig. 6 denote the mean effective variance of the ten synthetic fracture realizations and the shaded area represents one standard deviation upper and lower with respect to the mean. As can be seen from Fig. 6, the higher the $\sigma_1^\infty/\sigma_2^\infty$ is, the larger the effective variance is. In response to the previous magnitude and orientation difference analysis, we can observe that for the models subjected to higher $\sigma_1^\infty/\sigma_2^\infty$ and thus with larger overall stress variability, a larger difference between the Euclidean mean and far-field stress generally occurs. This difference and larger overall stress variability is caused by the re-activation of slipping between fracture walls due to higher differential stresses induced by larger far-field stress ratio, as demonstrated in [24]. In addition, the overall stress variability generally increase with the decreasing a, and the models with larger $\bar{\gamma}$ usually have larger overall stress variability. This is mainly due to the enhanced slipping accommodated along a large number of large fractures that are preferentially oriented for frictional sliding for models with smaller a and larger $\bar{\gamma}$ [24]. However, it seems the a and $\bar{\gamma}$ have no apparent influence on the difference between the Euclidean mean and far-field stress. Furthermore, the variation of the effective variance of the ten synthetic fracture realizations for each combination of a and $\bar{\gamma}$ decreases with the increasing a, especially for $\sigma_1^\infty/\sigma_2^\infty = 3$, which is consistent with the variation change of the difference between the Euclidean mean and far-field stress demonstrated earlier.

3.2. The natural fracture networks

We have conducted a total of 37 simulations on the Hornelen natural fracture network, i.e. one simulation for the far-field stress ratio

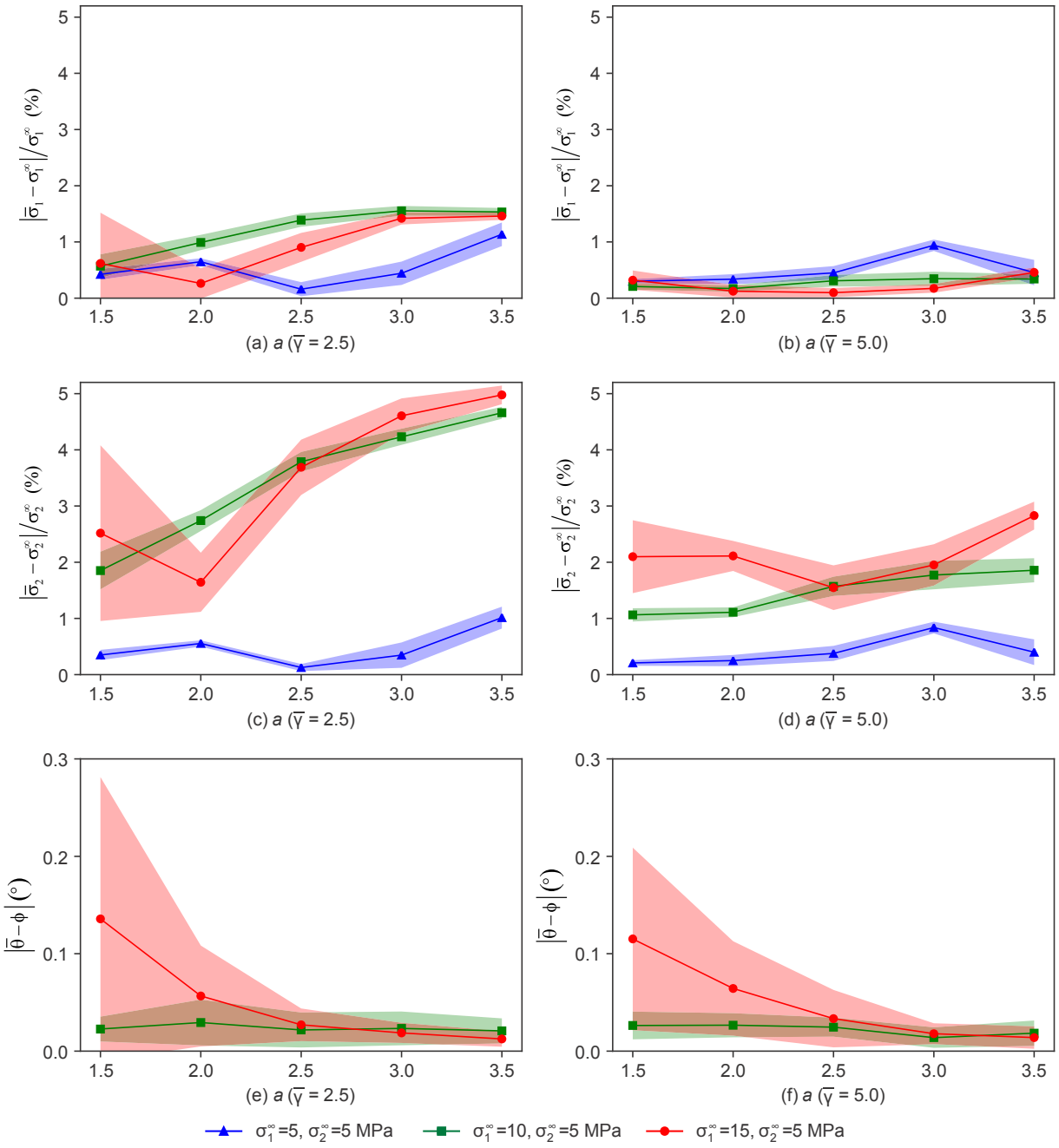

Fig. 5. The difference between the Euclidean mean of all simulated local stresses and the corresponding prescribed far-field stress in terms of principal stresses for the synthetic fracture rock mass models. The magnitude and orientation differences are shown in percentage and degree (°), respectively. Each marker represents the mean of the difference of the ten synthetic fracture realizations corresponding to a specific combination of a and $\bar{\gamma}$, and the associated shaded area represents one standard deviation upper and lower with respect to the mean. Note that the orientation difference is not calculated for $\sigma_1^\infty/\sigma_2^\infty = 1$ scenario.

$\sigma_1^\infty/\sigma_2^\infty = 1$ and 18 simulations (with different far-field stress loading angles) for $\sigma_1^\infty/\sigma_2^\infty = 2$ and 3, respectively. The distribution of major principal stress for some of the far-field stress orientation cases are presented in Fig. 7. The local stresses change with the rotation of the far-field stress, and we observe a higher degree of stress heterogeneity for the models subjected to larger $\sigma_1^\infty/\sigma_2^\infty$.

The differences between the Euclidean mean of all local stress data and the prescribed far-field stress for each model in terms of principal stress magnitude and orientation are shown in Fig. 8 with respect to the far-field stress orientation ϕ. Again, the Euclidean means of all local stresses are very close to the far-field stresses, with the largest differences for the major, minor principal stress magnitude and orientation being 1.0%, 2.7%, and 0.43°, respectively. Both the magnitude and orientation differences fluctuate with the far-field stress orientation ϕ. With the increasing $\sigma_1^\infty/\sigma_2^\infty$, the difference in terms of major principal stress magnitude decreases (Fig. 8a), whereas the difference in terms of minor principal stress magnitude generally shows an opposite trend (Fig. 8b). Similar to the synthetic fracture models, the difference between the Euclidean mean and far-field stress is negligible for the simulations subjected to $\sigma_1^\infty/\sigma_2^\infty = 1$; for $\sigma_1^\infty/\sigma_2^\infty = 2$ and 3 scenarios, the difference in terms of minor principal stress magnitude (Fig. 8b) are mainly larger than that of the major principal stress (Fig. 8a).

Likewise, the difference between the Euclidean mean and far-field stress may also be related to the stress variability. We calculate the effective variance of all simulated stresses in each Hornelen model and the results are presented in Fig. 9 with respect to the far-field stress

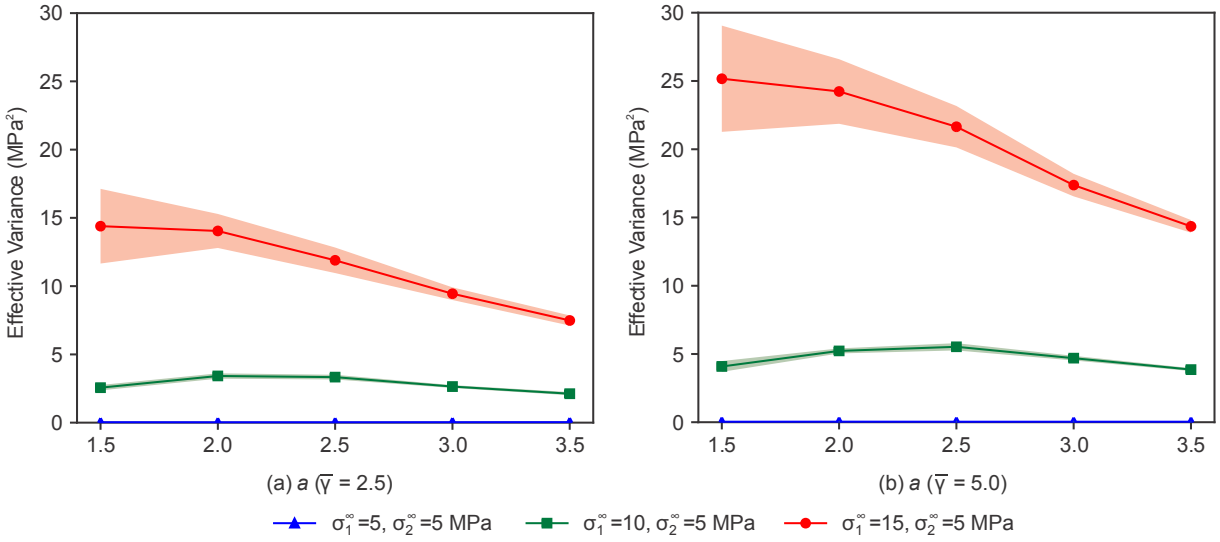

Fig. 6. The effective variance of all simulated stresses in each synthetic fracture model. Each marker represents the mean of the effective variance of the ten synthetic fracture realizations corresponding to a specific combination of a and $\bar{\gamma}$, and the corresponding shaded area represents one standard deviation upper and lower with respect to the mean.

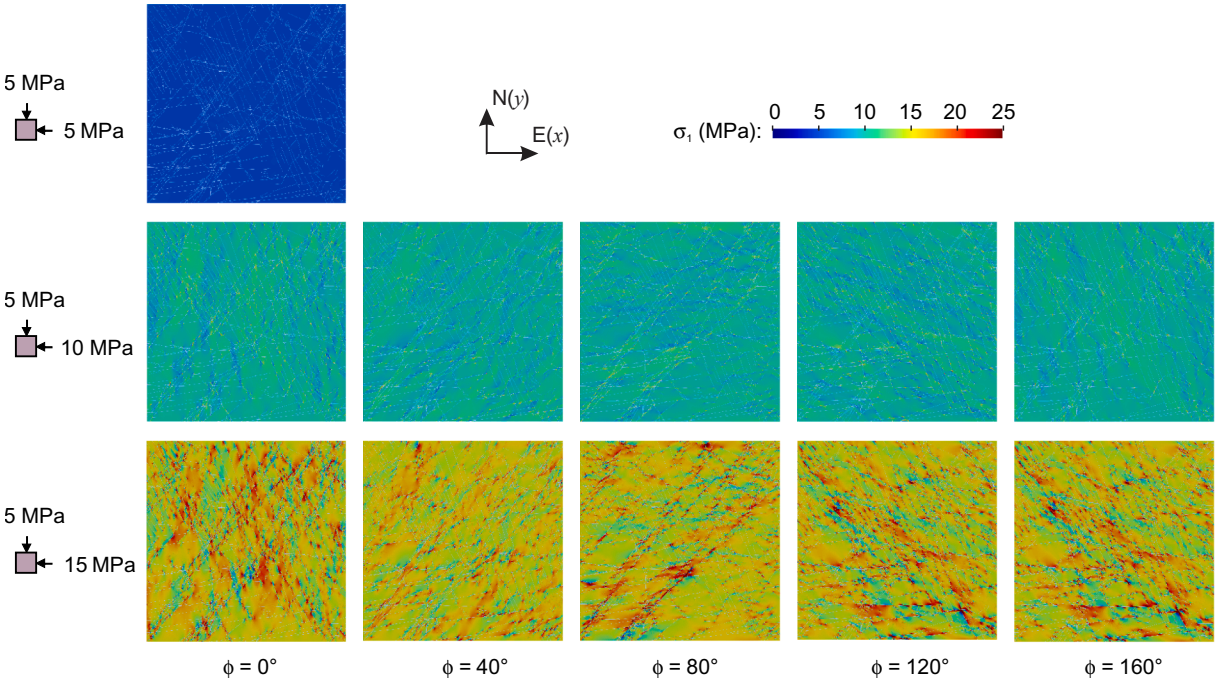

Fig. 7. Distributions of local major principal stresses in the Hornelen natural fracture network model under different far-field stress loading conditions imposed at different angles ϕ.

orientation ϕ. As can be seen from Fig. 9, the higher the $\sigma_1^\infty/\sigma_2^\infty$, the larger the overall stress variability for each model. Also, the maximum effective variance occurs around 10-20° and 100-110° for all the far-field stress scenarios, which are respectively the bisection orientations between fracture sets 40° and 150° (or, −30°) and between 85° and 150°. This is because of the anisotropic geometry of the Hornelen fracture system such that significant stress variability caused by shear displacements occurs when preferentially-oriented fractures are in favor of intense slipping when subjected to far-field stresses in such orientations [42]. Specifically, in case of ϕ = 10–20°, both the 40° and 150° (or, −30°) fracture sets have potential for higher slipping; in case of ϕ = 100–110°, both the 85° and 150° fracture sets are active in shear. This type of fracture slipping induced stress perturbation is intensified when the fractures are driven by higher differential stresses associated with larger far-field stress ratios. The large differences between the Euclidean mean of all simulated stress data and the far-field stress for each model, especially the magnitude difference (Fig. 8a & b), roughly agrees with the far-field stress orientations that have large overall stress variability, which suggests that the differences between the Euclidean mean and far-field stress may be related to the stress variability.

The same far-field stress scenarios are employed on the Kilve and Bristol fracture networks. The comparison between the Euclidean mean and far-field stress for these two models is presented in Appendix C and shows a mean magnitude difference less than 5% and mean orientation difference less than 1.0°. The small difference between the Euclidean mean of all local stress data and the prescribed far-field stress for the natural fracture network models, again, validates their equality. This further suggests that for a large amount of available local stress data,

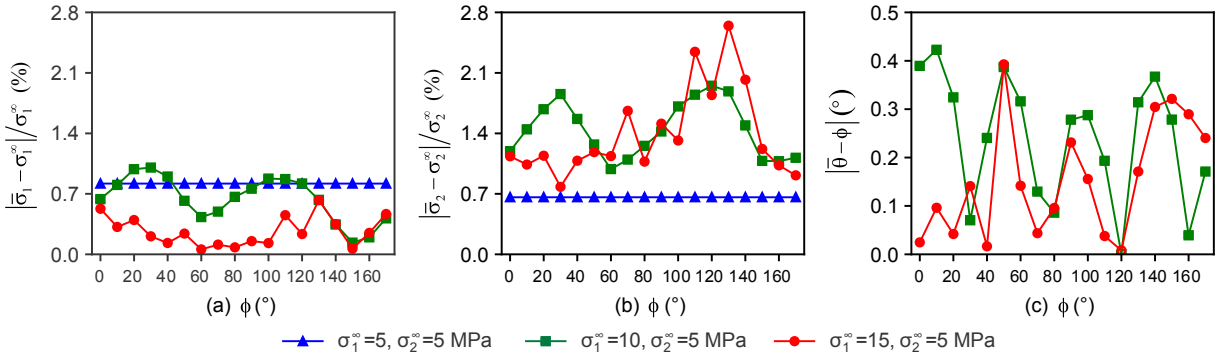

Fig. 8. The difference between the Euclidean mean of all simulated local stresses and the corresponding far-field stress with respect to the far-field stress orientation ϕ for the Hornelen models. The magnitude and orientation differences are shown in percentage and degree (°), respectively. Note that for the $\sigma_1^\infty/\sigma_2^\infty = 1$ scenario, the magnitude difference is duplicated for all far-field stress orientation cases for pure comparison purpose, and the orientation difference is not compared.

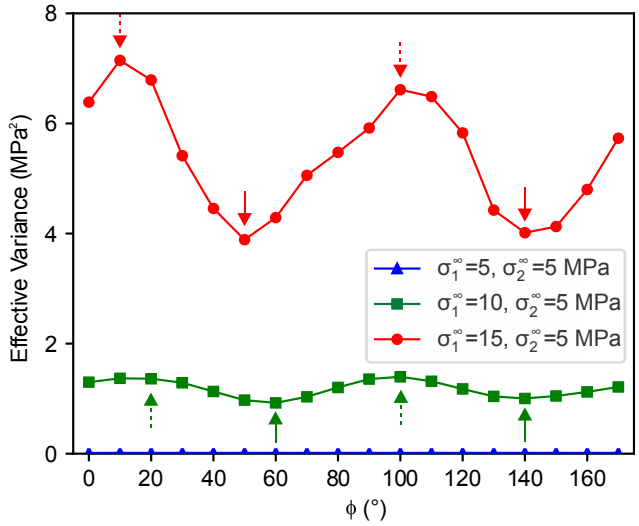

Fig. 9. The effective variance of all simulated stresses in each Hornelen model with respect to the far-field stress orientation ϕ. The small arrows (dashed and solid) indicate the local extrema.

the Euclidean mean gives a good approximation of the far-field stress. Additionally, this equality also supports our understanding of the principles of solid mechanics since, essentially, the mean stress represents the average effect of the far-field stress on the rock mass, and in order to maintain model equilibrium, the mean stress should be theoretically balancing the boundary loadings, i.e. equivalent to the far-field stress. However, due to implementation difficulties and budget limits, most rock engineering projects usually only conduct a limited number of *in situ* stress measurements. Thus, in the next section, we will examine whether the Euclidean mean can still give an acceptable estimate of the far-field stress state for limited *in situ* stress measurements.

4. Effect of sample size of local stress measurements on far-field stress estimation

To further explore the equality between the Euclidean mean and far-field stress for conditions when only a limited number of local stress data are available, for each of the synthetic and the Hornelen model, we randomly sample a certain number of stress tensors (say, from 5 to 50 with a step size of 5) from all the simulated local stresses, and then calculate their Euclidean mean and compare its principal stress magnitudes and orientation with the corresponding prescribed far-field stress. Here, we use 10% and 10° as the acceptable ranges for the magnitude and orientation difference, respectively. In other words, if the differences satisfy $|\bar{\sigma}_1 - \sigma_1^\infty|/\sigma_1^\infty \leqslant 10\%$, $|\bar{\sigma}_2 - \sigma_2^\infty|/\sigma_2^\infty \leqslant 10\%$ and $|\bar{\theta} - \phi| \leqslant 10°$ at the meantime, the Euclidean mean of the limited number of local stresses are considered to be a practically acceptable estimate of the far-field stress. For a specific sample size in each model, the sampling procedure is repeated 10,000 times so that a stable acceptance ratio can be achieved, which also gives the probability of the Euclidean mean of the specific number of local stresses as being a reasonable estimate of the far-field stress according to the aforementioned acceptance criterion. Additionally, to check the influence of stress variability on the sampling results, the acceptance ratio and the effective variance are also compared.

4.1. The synthetic fracture models

The sampling results which give the probability of Euclidean mean as being an acceptable estimate of the far-field stress for the synthetic fracture models with mean fracture intensity $\bar{\gamma} = 2.5\ \mathrm{m}^{-1}$ are presented in Fig. 10 for the three far-field stress ratios. Each marker denotes the mean of the acceptance probabilities of the ten synthetic fracture realizations corresponding to a specific combination of a and $\bar{\gamma}$, and the associated shaded area represents one standard deviation above and below the mean. It can be seen that, as the sample size increases, the probability of obtaining acceptable estimate of the far-field stress increases. However, when the sample size is beyond a certain value, further increase of the sample size only has a slight effect on the increase of acceptance probability. For example, for the models subjected to $\sigma_1^\infty/\sigma_2^\infty = 1$, the probability only witnesses a less than 10% increase when the sample size increases from 25 to 50 (Fig. 10a & d). With the increase of $\sigma_1^\infty/\sigma_2^\infty$, the probability shows an overall decreasing trend. Only a small probability change has been observed with respect to a, especially for $\sigma_1^\infty/\sigma_2^\infty = 1$ and 2, and the variability of the probability for each group of the ten synthetic fracture realizations (shaded area) is mainly less than 5%.

The probability of obtaining acceptable estimates of far-field stress has a close relationship with the overall stress variability characterized by the effective variance (Fig. 6a). A comparison between Fig. 10 and Fig. 6a suggests that larger acceptance probability generally occurs in the models with smaller effective variance. For example, the higher the ratio $\sigma_1^\infty/\sigma_2^\infty$ is, the larger the effective variance is and thus a smaller acceptance probability. Specifically, for the models subjected to $\sigma_1^\infty/\sigma_2^\infty = 1$, the effective variances are very small; as a result, relatively large probabilities can be seen in Fig. 10a & d. For $\sigma_1^\infty/\sigma_2^\infty = 2$, the effective variance first increases and then decreases with respect to a, with a maximum at $a = 2.5$. This is probably because the stress variability is governed by two types of perturbations: slipping along fractures and stress concentration at fracture tips. When a is small, the system accommodates significant shearing along large fractures. When a increases, the effect of slipping-induced stress perturbation is more suppressed and the stress concentration at fracture tips becomes dominant

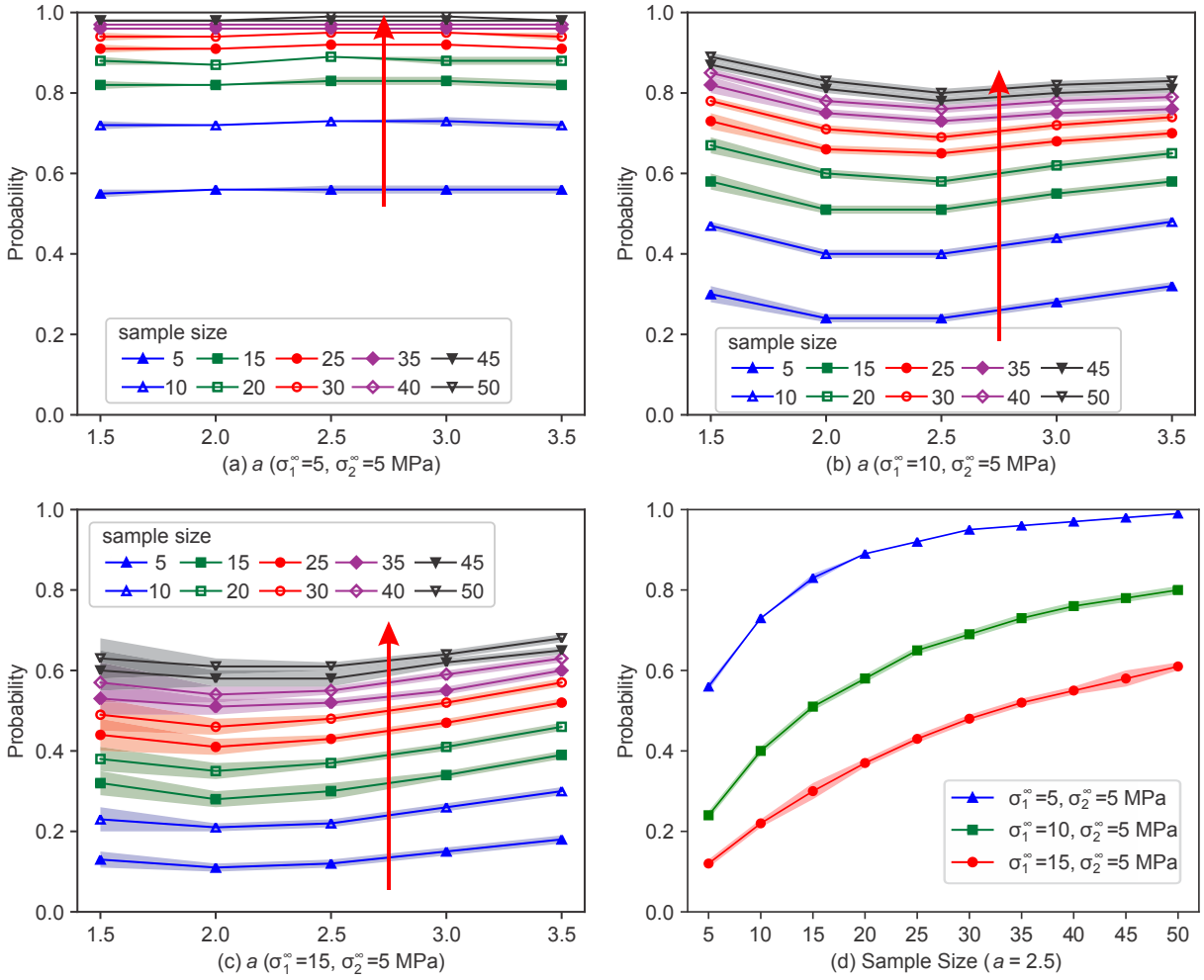

Fig. 10. The probability of obtaining acceptable far-field stress estimate based on the Euclidean mean of a limited number of local stresses for the synthetic fracture models with $\bar{\gamma} = 2.5\,\mathrm{m}^{-1}$. (a) $\sigma_1^\infty/\sigma_2^\infty = 1$, (b) $\sigma_1^\infty/\sigma_2^\infty = 2$, (c) $\sigma_1^\infty/\sigma_2^\infty = 3$, and (d) acceptance probability with respect to sample size for the models with $a = 2.5$ and subjected to the three far-field stress ratios. Note that (d) is a cross-section of (a–c) to facilitate comparison. Each marker represents the mean of the acceptance probabilities of the ten synthetic fracture realizations corresponding to a specific combination of a and $\bar{\gamma}$, and the corresponding shaded area represents one standard deviation upper and lower with respect to the mean. The vertical arrow in (a–c) indicates the increasing sample size.

due to the constraint of matrix against fracture shearing. The compromise of the two effects eventually leads to the maximum value at $a = 2.5$ when $\sigma_1^\infty/\sigma_2^\infty = 2$. Whereas for $\sigma_1^\infty/\sigma_2^\infty = 3$, because of the high differential stress, the slipping-induced stress perturbation is much more dominated. The acceptance probability shown in Fig. 10b is clearly in response to this trend, i.e. first decreases and then increases. The models subjected to $\sigma_1^\infty/\sigma_2^\infty = 3$ have a decreasing effective variance with respect to a (Fig. 6a), and thus the probability shows an increasing trend (Fig. 10c). Furthermore, for the models with small a and subjected to $\sigma_1^\infty/\sigma_2^\infty = 3$, the effective variance has a large variability (shaded area in Fig. 6a), which is manifested by the large variation of probability shown on the left-hand side of Fig. 10c.

The above trends for the acceptance probability change and the relationships between the acceptance probability and effective variance can also be observed for the synthetic fracture models with mean fracture intensity $\bar{\gamma} = 5.0\,\mathrm{m}^{-1}$, as presented in Fig. 6b for the effective variances and in Fig. 11 for the acceptance probabilities. However, the effective variance of the models with $\bar{\gamma} = 5.0\,\mathrm{m}^{-1}$ (Fig. 6b) is generally larger than the ones with $\bar{\gamma} = 2.5\,\mathrm{m}^{-1}$ (Fig. 6a), especially for the simulations under $\sigma_1^\infty/\sigma_2^\infty = 2$ and 3. Correspondingly, we can see a smaller acceptance probability (i.e. lower positions of the lines) in Fig. 11 than that in Fig. 10. Both Fig. 10 and Fig. 11 reveal that the larger the overall stress variability is (i.e. larger effective variance), the smaller the probability is for recovering far-field stress information based on a limited number of local stress measurements.

4.2. The Hornelen models

The sampling results for the Hornelen models with respect to the different far-field stress orientation ϕ are presented in Fig. 12. Again, the probability of obtaining an acceptable estimate of far-field stress increases with the increase of sample size, and the acceptance probability exhibits an overall decreasing trend when $\sigma_1^\infty/\sigma_2^\infty$ increases. For each sample size, the acceptance probability varies with the far-field stress orientation ϕ and displays a similar changing trend for the models subjected to both $\sigma_1^\infty/\sigma_2^\infty = 2$ and 3 (Fig. 12b & c), although the latter shows more distinct probability change.

The change of acceptance probability with respect to the far-field stress orientation ϕ has an opposite trend with the change of effective variance, which is similar to that of the previous synthetic fracture models. For example, for the models subjected to $\sigma_1^\infty/\sigma_2^\infty = 2$, the local maxima and minima of effective variance occur at $\phi = 20^\circ$ and 100°, and 60° and 140°, respectively (Fig. 9), and accordingly, the local minima and maxima of the acceptance probability can be found at $\phi = 20^\circ$ and 100°, and 60° and 140°, respectively (Fig. 12b). Similarly, the local minima and maxima of acceptance probability for the models

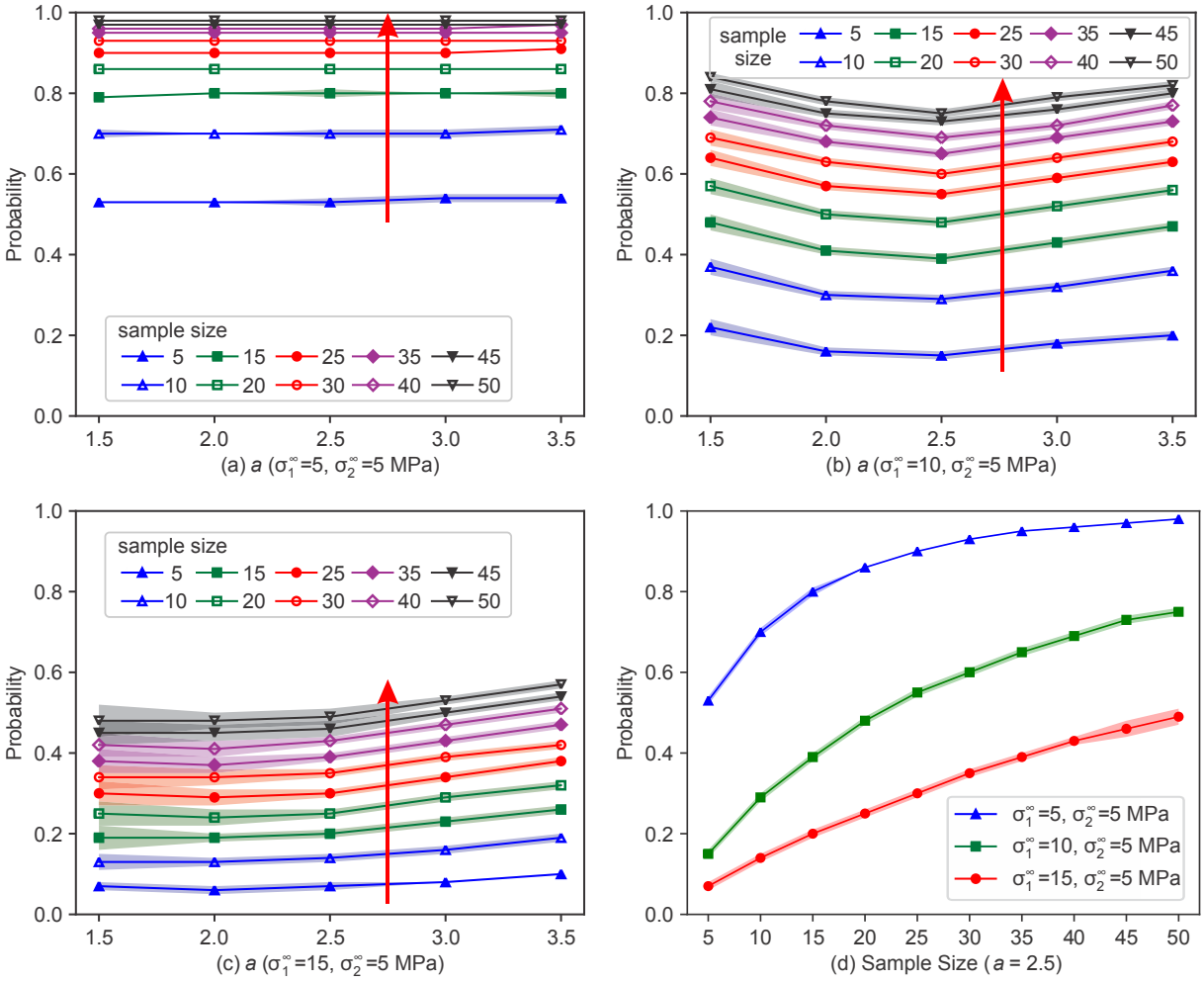

Fig. 11. The probability of obtaining acceptable far-field stress estimate based on the Euclidean mean of a limited number of local stresses for the synthetic fracture models with $\bar{\gamma} = 5.0\,\mathrm{m}^{-1}$. (a) $\sigma_1^\infty/\sigma_2^\infty = 1$, (b) $\sigma_1^\infty/\sigma_2^\infty = 2$, (c) $\sigma_1^\infty/\sigma_2^\infty = 3$, and (d) acceptance probability with respect to sample size for the models with $a = 2.5$ and subjected to the three far-field stress ratios. Note that (d) is a cross-section of (a–c) to facilitate comparison. Each marker represents the mean of the acceptance probabilities of the ten synthetic fracture realizations corresponding to a specific combination of a and $\bar{\gamma}$, and the corresponding shaded area represents one standard deviation upper and lower with respect to the mean. The vertical arrow in (a–c) indicates the increasing sample size.

subjected to $\sigma_1^\infty/\sigma_2^\infty = 3$ are seen at $\phi = 10^\circ$ and 100°, and 60° and 140°, respectively (Fig. 12c), and as shown in Fig. 9, the local maxima and minima of the effective variance are observed at the same places. Additionally, for $\sigma_1^\infty/\sigma_2^\infty = 3$, the large changing range of effective variance with respect to the far-field stress orientation (Fig. 9) explains the reason why the models under this far-field stress ratio show more distinct acceptance probability changes (Fig. 12c).

Both the synthetic and Hornelen models suggest that the effective variance, as a measure of the overall stress variability in fractured rock masses, seems to be a useful indicator of the probability of obtaining acceptable far-field stress estimate based on limited local measurements: the larger the effective variance is, the more stress measurements are needed in order to achieve a reliable far-field stress estimate. However, the number of stress measurements needed to obtain a practically acceptable far-field stress varies case by case. Taking the Hornelen model sampling results shown in Fig. 12 for example, if one wants to reach an 80% acceptability for far-field stress estimation, more than 20, 30 and 50 stress measurements are needed for the models subjected to $\sigma_1^\infty/\sigma_2^\infty = 1$, 2 and 3, respectively. While based on the synthetic fracture model results presented in Fig. 11, if one wants to reach the same acceptability, more than 15 and 40 stress measurements are required for $\sigma_1^\infty/\sigma_2^\infty = 1$ and 2, respectively; however, more than 50 stress measurements can only guarantee an acceptability of approximately 70% for $\sigma_1^\infty/\sigma_2^\infty = 3$.

Therefore, an important finding of the above analyses is that a practically acceptable far-field stress estimate often requires a large number of stress measurements. For the small number of stress measurements often conducted in rock engineering projects (generally less than 10) [52], taking the sampling results for synthetic and Hornelen models using the intermediate far-field stress ratio $\sigma_1^\infty/\sigma_2^\infty = 2$ for example, the probabilities of obtaining acceptable far-field stress estimate are around 40% and 50%, respectively. These small acceptance probability values suggest that simply using the average of very small number of stress measurements as input for further rock structure design and numerical analysis may have the potential to yield significantly erroneous results.

5. Conclusions and discussion

In this study, we have investigated the relationship between the Euclidean mean of local stresses and the far-field stress using the FDEM simulated stress fields of both synthetic fracture network following power-law length scaling and a natural fracture network extracted from real outcrops. We have used three sets of prescribed far-field stresses, and a total of 300 simulations and 111 simulations have been respectively conducted based on the synthetic and natural fracture models.

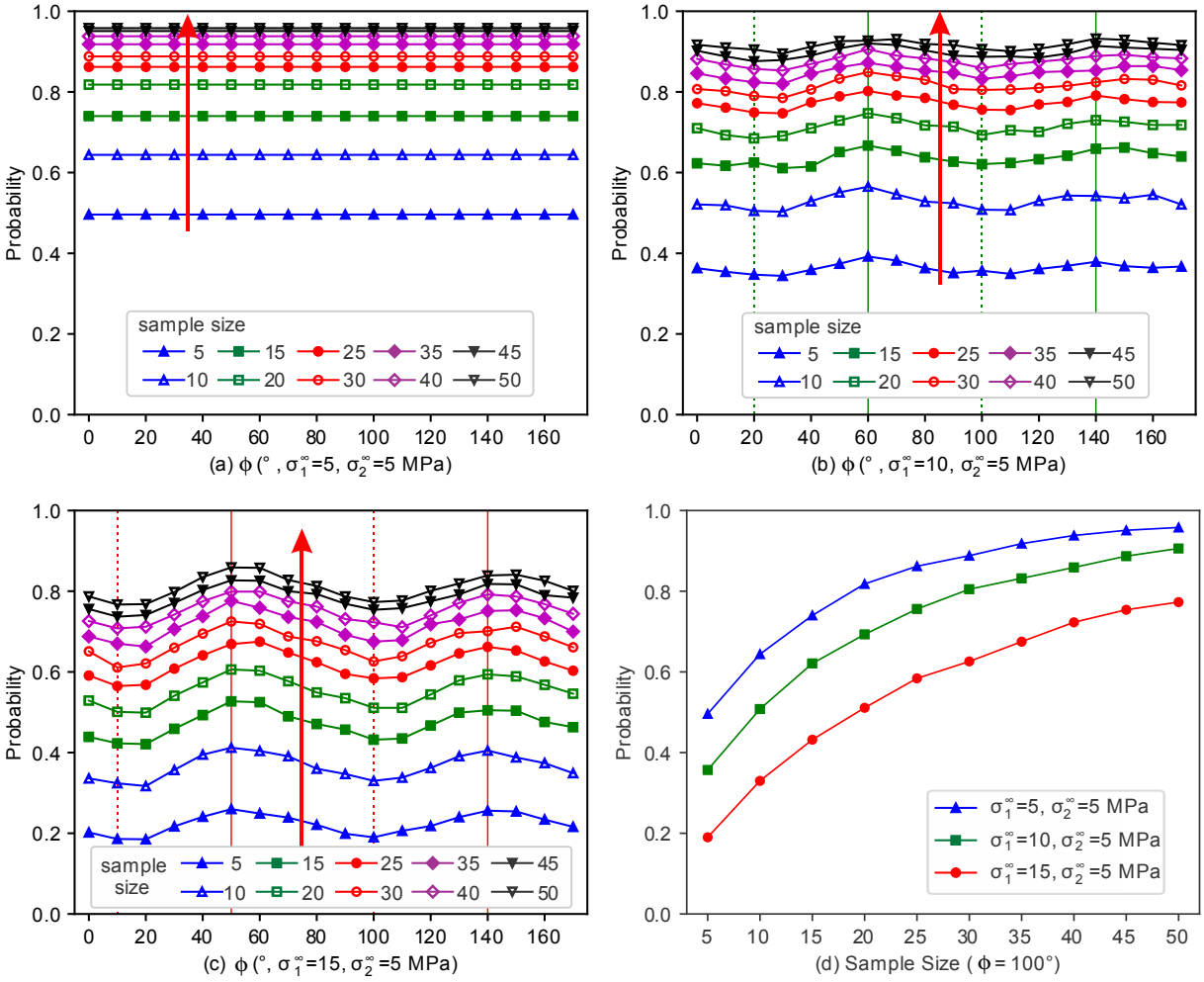

Fig. 12. The probability of obtaining acceptable far-field stress estimate based on the Euclidean mean of a limited number of local stresses for the Hornelen models. (a) $\sigma_1^\infty/\sigma_2^\infty = 1$, (b) $\sigma_1^\infty/\sigma_2^\infty = 2$, (c) $\sigma_1^\infty/\sigma_2^\infty = 3$, and (d) acceptance probability with respect to sample size for the models subjected to the three far-field stress ratios. Note that (d) is a cross-section of (a-c) to facilitate comparison. The vertical arrow indicates the increasing sample size. Note that for $\sigma_1^\infty/\sigma_2^\infty = 1$ scenario, the acceptance probability for each sample size in (a) is duplicated for all far-field stress orientations for pure comparison purpose. The vertical lines (dashed and solid) in (b) and (c) represent local extrema.

Upon the simulation reaches equilibrium, the Euclidean means of all simulated stress data and randomly sampled stress data have been calculated and compared with the prescribed far-field stress to examine whether the Euclidean mean of local stresses can give an acceptable estimate of the far-field stress.

The calculations show that when considering all the stress data in each model, for the synthetic fracture models, the magnitude difference between the Euclidean mean and the prescribed far-field stress is less than 5% and the orientation difference is smaller than 0.3°. Larger differences are seen for the models subjected to higher far-field stress ratio and thus with larger overall stress variability measured by the effective variance. For the Hornelen natural fracture models, the largest differences for the major, minor principal stress magnitude and orientation are 1.0%, 2.7%, and 0.43°, respectively. Both the magnitude and orientation differences fluctuate with the far-field stress orientation, and larger difference generally occurs for the model having higher overall stress variability. The insignificant difference between the Euclidean mean of all local stress data and the prescribed far-field stress for both the synthetic and natural fracture models demonstrates the equality between the two quantities, and this provides evidence that for a large amount of available local stress data, the Euclidean mean is a very close approximation of the far-field stress.

The sampling results demonstrate that for both the synthetic and natural fracture models the probability of obtaining an acceptable estimate of the far-field stress is increasing with the increasing sample size. Additionally, with the increasing $\sigma_1^\infty/\sigma_2^\infty$, the probability has an overall decreasing trend. This acceptance probability has a close relationship with the stress variability, i.e. the larger the stress variability is, the smaller the probability is for obtaining an acceptable far-field stress for a specific number of local stress measurements, and thus the more stress measurements are needed in practice.

Of great importance is our finding that a practically reliable far-field stress estimate often requires a large number of stress measurements. For the small number of stress measurements often conducted in rock engineering projects, simply using their average as input far-field stress for further rock structure design and numerical analysis may yield significantly misleading results. In order for robust stress-related analysis, we suggest combining the numerical simulations and local stress measurements to reach more detailed stress fields through careful calibrations, such as using the recently proposed geomechanical-numerical model [53–55]. Nevertheless, calculating the Euclidean mean of local stress measurements is a correct direction for achieving reliable far-field stress.

Appendix A. List of main symbols

a	power-law length exponent
l	fracture length
D	fractal dimension
$n(l,L)$	probability density function of fracture length
α	density term
$\bar{\gamma}$	mean fracture intensity
$\mathbf{S}_i$	ith stress tensor, $i = 1, 2, \ldots n$
$\bar{\mathbf{S}}$	euclidean mean stress tensor
$\bar{\sigma}_1$	major principal stress of the Euclidean mean stress tensor
σ_1^{∞}	major far-field stress
$\bar{\sigma}_2$	minor principal stress of the Euclidean mean stress tensor
σ_2^{∞}	minor far-field stress
ϕ	orientation of σ_1^{∞}
$\bar{\theta}$	orientation of $\bar{\sigma}_1$

Appendix B. Effective variance – scalar-valued measure of stress variability

Stress in rock often displays significant variability, and it is important that the overall variability of stress can be characterized in a quantitative manner [23,24,51,56]. Dispersion, which denotes how scatter or spread out a data group is, is an effective parameter for such characterization. Since it has been demonstrated that the variability of stress tensors can be adequately represented by the variability of its distinct tensor components in a multivariate statistics manner [57], we have proposed using the widely-used concept of "effective variance" in multivariate statistics for group dispersion measure in [58] as a scalar-valued measure of the overall stress variability [23,24,51].

The effective variance of stress tensors can be calculated based on the covariance matrix of their distinct tensor components referred to a common Cartesian coordinate system. For a stress tensor denoted in Eq. (4), its distinct tensor components are

$$\mathbf{s}_{\mathrm{d}} = \mathrm{vech}(\mathbf{S}) = [\sigma_x \quad \tau_{yx} \quad \sigma_y]^T. \tag{B.1}$$

Here, the subscript "d" denotes "distinct", $[\,\cdot\,]^T$ represents the matrix transpose, and $\mathrm{vech}(\cdot)$ is the half–vectorization function which stacks only the lower triangular (i.e. on and below the diagonal) columns of a tensor into column vector containing only its distinct components [[59], p. 246]. For the stress vector $\mathbf{s}_{\mathrm{d}}$, its covariance matrix is

$$\mathbf{\Omega} = \mathrm{cov}(\mathbf{s}_{\mathrm{d}}) = \frac{1}{n}\sum_{i=1}^{n}(\mathbf{s}_{\mathrm{d}_i} - \bar{\mathbf{s}}_{\mathrm{d}})\cdot(\mathbf{s}_{\mathrm{d}_i} - \bar{\mathbf{s}}_{\mathrm{d}})^T, \tag{B.2}$$

where $\bar{\mathbf{s}}_{\mathrm{d}}$ denotes the mean vector and can be calculated by

$$\bar{\mathbf{s}}_{\mathrm{d}} = \frac{1}{n}\sum_{i=1}^{n}\mathbf{s}_{\mathrm{d}_i}. \tag{B.3}$$

Based on the covariance matrix $\mathbf{\Omega}$ given in Eq. (B.2), the effective variance is defined as

$$V_{\mathrm{e|d}} = \frac{1}{2}\sqrt[p(p+1)]{|\mathbf{\Omega}|}, \tag{B.4}$$

where $|\cdot|$ denotes the matrix determinant and $p(p = 2)$ is the dimension of the stress tensor. Similar to the variance and standard deviation of scalar data, the smaller the effective variance, the more uniform the stress data would be. The effective variance has proven its effectiveness for stress variability characterization in many recent work [23,24,56,60].

Appendix C. Equality between Euclidean mean and far-field stress examined based on two additional natural fracture networks

In terms of natural fracture network, in addition to the Hornelen model, we have employed two additional models – the Kilve and Bristol fracture networks (Fig. C1) – to further validate the equality between the Euclidean mean of all simulated stress data and the prescribed far-field stress. The Kilve and Bristol model are obtained based on the outcrops of limestone beds located on the southern margin of the Bristol Channel Basin, UK [61,62], and their sizes are of $6 \times 6\,\mathrm{m}^2$ and $8 \times 8\,\mathrm{m}^2$, respectively. The material properties of the limestone rocks are assumed as follows: the bulk density is $2{,}700\,\mathrm{kg/m}^3$, the Young's modulus is 30.0 GPa, the Poisson's ratio is 0.27, the internal friction coefficient is 1.0, the tensile strength is 20.0 MPa, the cohesive strength is 40.0 MPa, the joint friction coefficient is 0.85, and the mode I and II energy release rates are 158.4 and 198.0 $\mathrm{J/m}^2$, respectively. Similar to the Hornelen model, three far-field stress scenarios are explored: (i) $\sigma_1^{\infty} = 5.0$ MPa, $\sigma_2^{\infty} = 5.0$ MPa, (ii) $\sigma_1^{\infty} = 10.0$ MPa, $\sigma_2^{\infty} = 5.0$ MPa, and (iii) $\sigma_1^{\infty} = 15.0$ MPa, $\sigma_2^{\infty} = 5.0$ MPa, and a series of simulations are conducted by rotating the far-field stresses clockwise for 170° with a step size of 10°, as demonstrated in Fig. 3b. Therefore, a total of 37 simulations are conducted for each fracture network.

When the models reach equilibrium, the differences between the Euclidean mean of all simulated stress data and the prescribed far-field stress for each model are compared using the approaches demonstrated in Section 3. Then the differences between the Euclidean mean and far-field stress for the 18 rotation scenarios under each prescribed far-field stress are averaged and the results are collected in Fig. C2 with their standard deviations. As can be seen that for the Kilve and Bristol models, the average differences between the Euclidean mean and far-field stress in terms of major, minor principal stress magnitude and orientation are less than 4.0%, 5%, and 1.0°, respectively. Although these differences are slightly higher than the ones for Hornelen models (Section 3.2), they validate the equality between the Euclidean mean and far-field stress in natural fracture networks. This again suggests that for a large amount of available local stress data, the Euclidean mean gives a good approximation of the far-field stress.

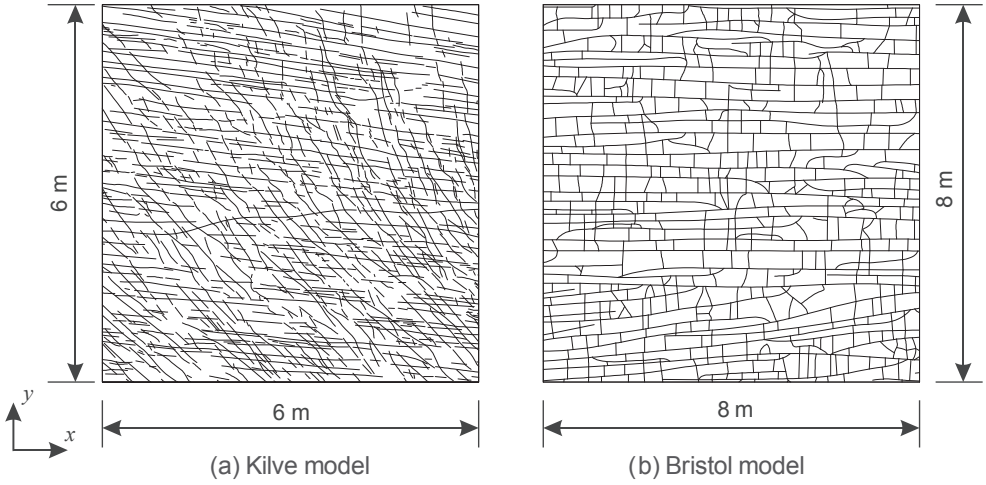

Fig. C1. The geometry of the Kilve and Bristol fracture networks.

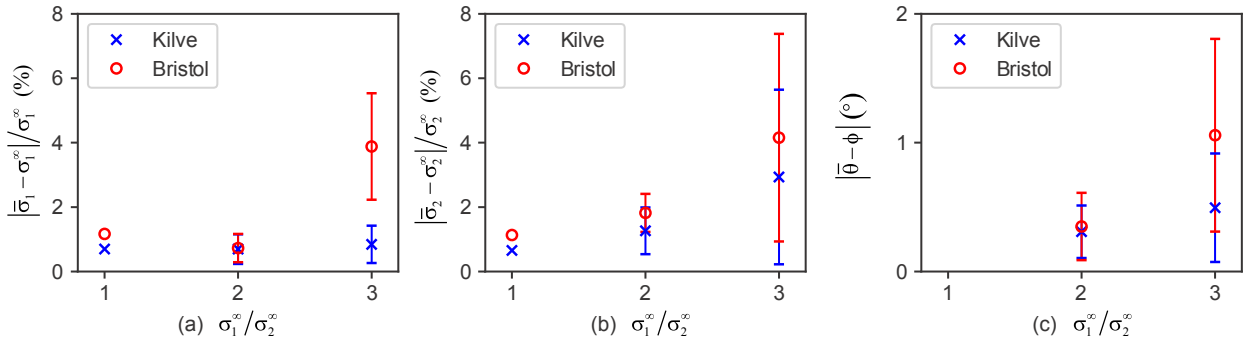

Fig. C2. The differences between the Euclidean mean and far-field stress for both the Kilve and Bristol models. Each marker represents the mean value of the 18 rotation scenarios of a specific prescribed far-field stress, and the error bar indicates the corresponding ± 1 standard deviation. Note that for $\sigma_1^\infty/\sigma_2^\infty = 1$ scenario, the magnitude differences between the Euclidean mean and far-field stress are not averaged, and the orientation difference is not compared.

References

[1] Amadei B, Stephansson O. Rock stress and its measurement. London: Springer; 1997.
[2] Zoback MD. Reservoir geomechanics. Cambridge: Cambridge University Press; 2010.
[3] Latham J-P, Xiang J, Belayneh M, Nick HM, Tsang C-F, Blunt MJ. Modelling stress-dependent permeability in fractured rock including effects of propagating and bending fractures. Int J Rock Mech Min Sci 2013;57:100–12.
[4] Zang A, Stephansson O. Stress field of the Earth's crust. Berlin: Springer; 2010.
[5] Zoback ML. First- and second-order patterns of stress in the lithosphere: the world stress map project. J Geophys Res Solid Earth 1992;97:11703–28.
[6] Guo P, Yao L, Ren D. Simulation of three-dimensional tectonic stress fields and quantitative prediction of tectonic fracture within the Damintun Depression, Liaohe Basin, northeast China. J Struct Geol 2016;86:211–23.
[7] Hudson JA, Feng X-T. Variability of in situ rock stress. In: Xie F, editor. Rock stress and earthquakes – proc 5th int symp on in-situ rock stress. Beijing, China: CRC Press; 2010. p. 3–10.
[8] Karatela E, Taheri A, Xu C, Stevenson G. Study on effect of in-situ stress ratio and discontinuities orientation on borehole stability in heavily fractured rocks using discrete element method. J Petrol Sci Eng 2016;139:94–103.
[9] Su S, Stephansson O. Effect of a fault on in situ stresses studied by the distinct element method. Int J Rock Mech Min Sci 1999;36:1051–6.
[10] Schmitt DR, Currie CA, Zhang L. Crustal stress determination from boreholes and rock cores: fundamental principles. Tectonophysics 2012;580:1–26.
[11] Homberg C, Hu JC, Angelier J, Bergerat F, Lacombe O. Characterization of stress perturbations near major fault zones: insights from 2-D distinct-element numerical modelling and field studies (Jura mountains). J Struct Geol 1997;19:703–18.
[12] Lei Q, Latham J-P, Tsang C-F. The use of discrete fracture networks for modelling coupled geomechanical and hydrological behaviour of fractured rocks. Comput Geotech 2017;85:151–76.
[13] Hudson JA, Harrison JP. Engineering rock mechanics – an introduction to the principles. Oxford: Elsevier; 1997.
[14] Lei Q, Latham J-P, Xiang J, Tsang C-F, Lang P, Guo L. Effects of geomechanical changes on the validity of a discrete fracture network representation of a realistic two-dimensional fractured rock. Int J Rock Mech Min Sci 2014;70:507–23.
[15] Wu Z, Wong LNY. Frictional crack initiation and propagation analysis using the numerical manifold method. Comput Geotech 2012;39:38–53.
[16] Zhao Z, Jing L, Neretnieks I, Moreno L. Numerical modeling of stress effects on solute transport in fractured rocks. Comput Geotech 2011;38:113–26.
[17] He P, Li S-c, Li L-p, Zhang Q-q, Xu F, Chen Y-j. Discontinuous deformation analysis of super section tunnel surrounding rock stability based on joint distribution simulation. Comput Geotech 2017;91:218–29.
[18] Martin CD. Characterizing in situ stress domains at the AECL Underground Research Laboratory. Can Geotech J 1990;27:631–46.
[19] Obara Y, Sugawara K. Updating the use of the CCBO cell in Japan: overcoring case studies. Int J Rock Mech Min Sci 2003;40:1189–203.
[20] Matsumoto S, Katao H, Iio Y. Determining changes in the state of stress associated with an earthquake via combined focal mechanism and moment tensor analysis: application to the 2013 Awaji Island earthquake, Japan. Tectonophysics 2015;649:58–67.
[21] Day-Lewis AD. Characterization and modeling of in situ stress heterogeneity PhD thesis California, USA: Stanford University; 2008.
[22] Hyett AJ. Numerical and experimental modelling of the potential state of stress in a naturally fractured rock mass PhD. Thesis London, UK: University of London; 1990.
[23] Gao K, Lei Q. Influence of boundary constraints on stress heterogeneity modelling. Comput Geotech 2018;99:130–6.
[24] Lei Q, Gao K. Correlation between fracture network properties and stress variability in geological media. Geophys Res Lett 2018;45.
[25] Gao K. Contributions to tensor-based stress variability characterisation in rock mechanics PhD thesis Canada: University of Toronto; 2017.
[26] Gao K, Harrison JP. Mean and dispersion of stress tensors using Euclidean and Riemannian approaches. Int J Rock Mech Min Sci 2016;85:165–73.
[27] Gao K, Harrison JP. Examination of mean stress calculation approaches in rock mechanics. Rock Mech Rock Eng 2019;52:83–95.
[28] Munjiza AA. The combined finite-discrete element method. London: John Wiley & Sons; 2004.
[29] Xiang J, Munjiza A, Latham J-P. Finite strain, finite rotation quadratic tetrahedral element for the combined finite–discrete element method. Int J Numer Meth Eng 2009;79:946–78.
[30] Xiang J, Munjiza A, Latham J-P, Guises R. On the validation of DEM and FEM/DEM

models in 2D and 3D. Eng Comput 2009;26:673–87.
[31] Yan C, Jiao Y-Y, Zheng H. A fully coupled three-dimensional hydro-mechanical finite discrete element approach with real porous seepage for simulating 3D hydraulic fracturing. Comput Geotech 2018;96:73–89.
[32] Yan C, Zheng H. A coupled thermo-mechanical model based on the combined finite-discrete element method for simulating thermal cracking of rock. Int J Rock Mech Min Sci 2017;91:170–8.
[33] Yan C, Zheng H, Sun G, Ge X. Combined finite-discrete element method for simulation of hydraulic fracturing. Rock Mech Rock Eng 2016;49:1389–410.
[34] Guo L. Development of a three-dimensional fracture model for the combined finite-discrete element method PhD. thesis London, UK: Imperial College London; 2014.
[35] Munjiza A, Andrews KRF, White JK. Combined single and smeared crack model in combined finite-discrete element analysis. Int J Numer Meth Eng 1999;44:41–57.
[36] Bonnet E, Bour O, Odling NE, Davy P, Main I, Cowie P, et al. Scaling of fracture systems in geological media. Rev Geophys 2001;39:347–83.
[37] Mayer J, Hamdi P, Stead D. A modified discrete fracture network approach for geomechanical simulation. Proceedings of the 1st international conference on discrete fracture network engineering. 2014.
[38] Byerlee J. Friction of rocks. Pure Appl Geophys 1978;116:615–26.
[39] Mahabadi OK. Investigating the influence of micro-scale heterogeneity and microstructure on the failure and mechanical behaviour of geomaterials PhD. thesis Canada: University of Toronto; 2012.
[40] Odling NE. Scaling and connectivity of joint systems in sandstones from western Norway. J Struct Geol 1997;19:1257–71.
[41] Pollard DD, Segall P. Theoretical displacements and stresses near fractures in rock: with applications to faults, joints, veins, dikes, and solution surfaces. In: Atkinson BK, editor. Fracture mechanics of rock. London: Academic Press; 1987. p. 277–349.
[42] Lei Q, Gao K. A numerical study of stress variability in heterogeneous fractured rocks. Int J Rock Mech Min Sci 2019;113:121–33.
[43] Brown ET, Hoek E. Trends in relationships between measured in-situ stresses and depth. Int J Rock Mech Min Sci Geomech Abs 1978;15:211–5.
[44] Herget G. Stresses in rock. Rotterdam: Balkema; 1988.
[45] Lisle RJ. The statistical analysis of orthogonal orientation data. J Geol 1989;97:360–4.
[46] Martin CD. Quantifying in situ stress magnitudes and orientations for Forsmark: Forsmark stage 2.2, R-07-26. Sweden: SKB; 2007.
[47] Zhao XG, Wang J, Cai M, Ma LK, Zong ZH, Wang XY, et al. In-situ stress measurements and regional stress field assessment of the Beishan area, China. Eng Geol 2013;163:26–40.
[48] Bulmer MG. Principles of statistics. New York: Dover Publications; 1979.
[49] Mardia KV. Statistics of directional data. London: Academic Press; 1972.
[50] Hudson JA, In Cooling CM. Situ rock stresses and their measurement in the U.K.—Part I. The current state of knowledge. Int J Rock Mech Min Sci Geomech Abs 1988;25:363–70.
[51] Gao K, Harrison JP. Scalar-valued measures of stress dispersion. Int J Rock Mech Min Sci 2018;106:234–42.
[52] Feng Y, Bozorgzadeh N, Harrison JP. Investigating the effect of sample size on uncertainty in stress estimations. 52nd U.S. rock mechanics/geomechanics symposium. Seattle, Washington: American Rock Mechanics Association; 2018.
[53] Ziegler MO, Heidbach O, Reinecker J, Przybycin AM, Scheck-Wenderoth M. A multi-stage 3-D stress field modelling approach exemplified in the Bavarian Molasse Basin. Solid Earth 2016;7:1365–82.
[54] Hergert T, Heidbach O, Reiter K, Giger SB, Marschall P. Stress field sensitivity analysis in a sedimentary sequence of the Alpine foreland, northern Switzerland. Solid Earth 2015;6:533–52.
[55] Ziegler MO. Manual of the matlab script FAST calibration v1.0, WSM technical report 18–01. GFZ German Research Centre for Geosciences; 2018.
[56] Gao K, Harrison JP. Generation of random stress tensors. Int J Rock Mech Min Sci 2017;94:18–26.
[57] Gao K, Harrison JP. Multivariate distribution model for stress variability characterisation. Int J Rock Mech Min Sci 2018;102:144–54.
[58] Peña D, Rodríguez J. Descriptive measures of multivariate scatter and linear dependence. J Multivariate Anal 2003;85:361–74.
[59] Seber GA. A matrix handbook for statisticians. New York: John Wiley & Sons; 2007.
[60] Gao K, Harrison JP. Re-examination of the in situ stress measurements on the 240 level of the AECL's URL using tensor-based approaches. Rock Mech Rock Eng 2018;51:3179–88.
[61] Belayneh MW, Matthai SK, Blunt MJ, Rogers SF. Comparison of deterministic with stochastic fracture models in water-flooding numerical simulations. AAPG Bull 2009;93:1633–48.
[62] Belayneh M, Cosgrove JW. Fracture-pattern variations around a major fold and their implications regarding fracture prediction using limited data: an example from the Bristol Channel Basin. Geol. Soc. Lond. Spec. Publ. 2004;231:89.